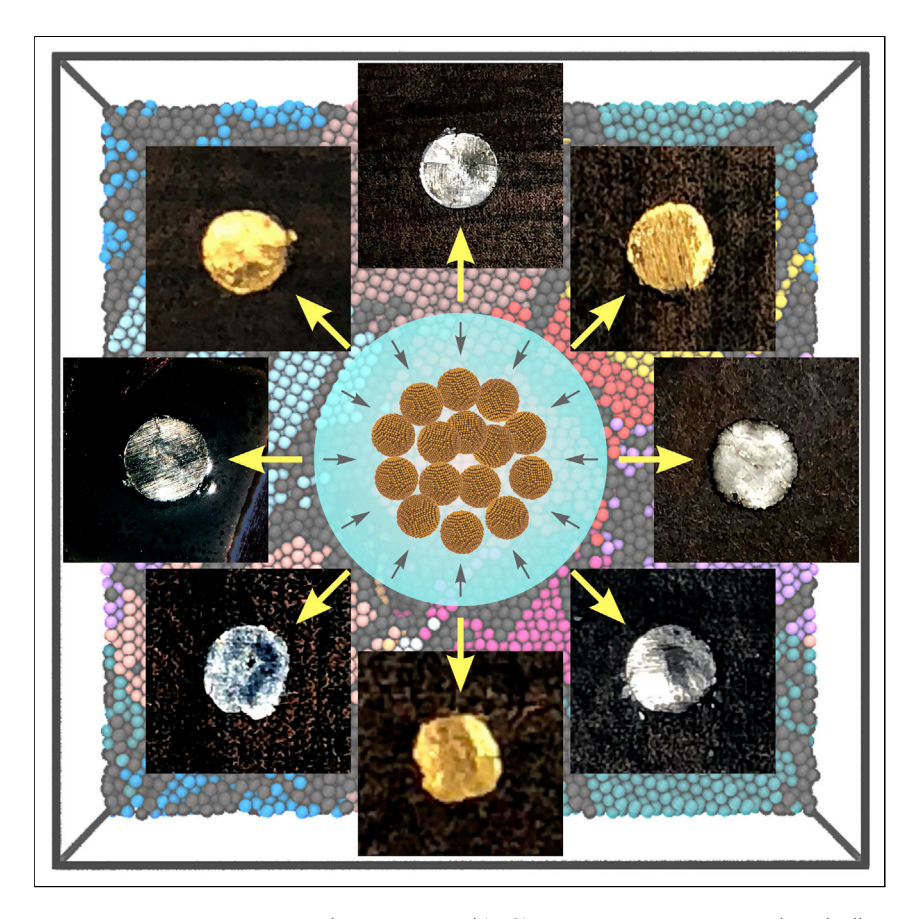




Article

Bulk Grain-Boundary Materials from Nanocrystals



We propose a new concept, the nanocrystal (NC)-coining process, to produce bulk materials with precisely tailored nanoscale grain-boundary conditions. By consolidating surface-engineered NCs into bulk materials using pressure, we can fabricate free-standing NC coins with metallic appearance and conductivity, while preserving the original NC domain feature. The obtained NC coins show enhanced mechanical hardness due to the Hall-Petch effect. With this method, we have created the first example of a bulk single-component metallic glass from amorphous palladium nanoparticles.

Yasutaka Nagaoka, Masayuki Suda, Insun Yoon, ..., Michael Grünwald, Hiroshi M. Yamamoto, Ou Chen

ouchen@brown.edu

HIGHLIGHTS

Fabrication of bulk grainboundary materials from eight kinds of metal nanoparticles

Precise nanoscale grain-boundary engineering using nanocrystals

Emerging the Hall-Petch effect to enhance mechanical hardness of the materials

The first example of a singlecomponent bulk metallic glass



Nagaoka et al., Chem 7, 1–17 February 11, 2021 © 2020 Elsevier Inc. https://doi.org/10.1016/j.chempr.2020.12.026 Chem



Article

Bulk Grain-Boundary Materials from Nanocrystals

Yasutaka Nagaoka,¹ Masayuki Suda,² Insun Yoon,³ Na Chen,¹ Hanjun Yang,¹ Yuzi Liu,⁴ Brendan A. Anzures,⁵ Stephen W. Parman,⁵ Zhongwu Wang,⁶ Michael Grünwald,⁷ Hiroshi M. Yamamoto,² and Ou Chen^{1,8,*}

SUMMARY

Grain-boundary engineering is pivotal to fully utilize the mechanical, electrical, and thermal-transport properties of various materials. However, current methods in metallurgy rely almost exclusively on top-down approaches, making precise grain-boundary engineering, especially at nanoscale, difficult to achieve. Herein, we report a method to produce tailored grain-boundary conditions with nanoscale precision from colloidal metal nanocrystals through surface treatment followed by a pressure-sintering process. The resulting bulk grain-boundary materials (which we call "nanocrystal coins") possess a metal-like appearance and conductivity while inheriting the original domain features of the nanocrystal building blocks. Nanoindentation measurements confirmed the superior mechanical hardness of the obtained materials. Further, we use this method to fabricate, for the first time, a single-component bulk metallic glass from amorphous palladium nanoparticles. Our discovery may spur the development of new materials whose functionality crucially depends on the domain configuration at nanoscale, such as superhard materials, thermoelectric generators, and functional electrodes.

INTRODUCTION

Grain boundaries (GBs) are an essential factor for a range of chemical, physical, and mechanical material properties, such as ductility, thermal and electric conductivity, and catalytic ability. 1-8 GB engineering had been practiced long before it was supported by scientific evidence. For example, metalsmiths have used various techniques, including quench hardening and "striking while the iron is hot" to harden metals, and these processes now are known as GB strengthening or the Hall-Petch effect. 9,10 From these primitive techniques, in more recent efforts, scientists have focused on developing systematic structure-property relationships that link GB conditions to improved material properties. 1-12 However, current methods of GB engineering rely largely on "top-down" approaches, such as electrodeposition, hammering, mechanical alloying, ⁷ rapid cooling, ⁵ and sputtering. ⁶ These methods do not allow precise control of a material's GB configuration, posing a severe challenge for the advancement of GB materials in practical applications. In this regard, pressure sintering of nanocrystals (NCs) is an intriguing "bottom-up" alternative to the top-down approaches. 13-23 External pressure can fuse individual NCs while largely preserving their original crystal domains. 13,16,18,20,21 However, in most previous efforts, adequate NC-sintering pressures (i.e., >10 GPa) were generated by diamond anvil cells, which severely limit the dimensions of the processable sample to hundreds of micrometers in lateral directions. Furthermore, pressure sintering in diamond anvil cells has resulted in low-dimensional nanostructures, 22 including nanorods, 20 nanowires, 13,16,21 and nanoplatelets, 14,17,19 yet to be extended to bulk-size materials.

The Bigger Picture

Enhancing materials' properties through grain-boundary (GB) engineering has been broadly employed in various scenes, ranging from an ancient "striking while the iron is hot" approach to modern state-of-the-art techniques. However, precisely controlling the GB condition of bulk materials at the nanometer scale has proven to be extremely challenging. In this work, we discover a new GB engineering approach, i.e., a nanocrystal (NC)coining process, through consolidating premade NCs into bulk GB materials under pressure. By using surface-engineered metal NCs as the building blocks of "nanograins," free-standing metal pieces (which we call "NC coins") with designed nanometersized domains can be produced. These NC coins show metallic appearance, conductivity, and enhanced mechanical hardness. Our method allows us to create the first single-component bulk metallic glass from amorphous palladium nanoparticles.





Here, we report a pressure-sintering method that transforms metal NCs into freestanding, sub-centimeter-scale, bulk GB materials. Our method relies on the surface modification of NCs by an inorganic-ligand exchange followed by a ligand removal. The resulting NCs are essentially bare and can be sintered at pressures as low as \sim 0.6 GPa. To demonstrate the versatility of this approach, we fabricated a set of sub-centimeter-scale GB-engineered "NC coins" from different metal NCs with various sizes, shapes, and compositions. These NC coins possess metallic features in terms of metallic luster and electrical conductivity but maintain the crystal domain features of the pristine NCs. Nanoindentation measurements unveiled that the NC coins had large hardness values due to the Hall-Petch effect. Importantly, we apply this method to create a bulk metallic glass through the sintering of amorphous palladium (Pd) nanoparticles (NPs). To the best of our knowledge, this is the first example of single-component bulk metallic glass generated under nonharsh conditions. We expect that our study will enable the development of detailed structure-property relationships for GB materials and pave the way toward the practical fabrication of bulk GB materials at an industrial scale.

RESULTS AND DISCUSSION

Creation of Bulk GB NC Coins

The bottom-up fabrication of GB materials through what we call the "NC-coining" process involves a ligand exchange of the synthesized metal NCs to replace the native organic capping ligands with small inorganic ones, ^{24,25} followed by removals of ligand and solvent through washing and drying processes. The resulting solid NC powder can then be processed by pressure sintering to generate the final bulk GB NC coins. 13-23 In the following, we describe the process for the case of gold NCs. (See the Methods section and Methods S1 for details.) A toluene solution of 1-dodecanethiol (DDT) capped small gold NCs (6.5 nm in diameter) was mixed with a (NH₄)₂S dimethyl sulfoxide (DMSO) solution in equal volumes to initiate the ligand-exchange reaction (Figures 1A and 1B; see also Figures S1 and S2; Table S1). After the ligand exchange was complete, the obtained S^{2-} -capped gold NCs were thoroughly purified by extraction using hexane and toluene, followed by washing with acetone and DMSO to remove the inorganic ligands and residual organic molecules (e.g., DDT), making the NC surfaces almost bare (Figures S2 and S3; Tables S1 and S2). Next, the gold NCs were thoroughly dried under vacuum conditions, resulting in a black NC powder (Figure 1C; see also Figure S4). Finally, the NC powder was loaded in a homemade piston cylinder and sintered at a pressure of ~0.6 GPa (see Methods S2), yielding a free-standing, dense, sub-centimeter-scale pellet, i.e., a gold NC coin (Figure 1D; see also Figures S5–S7). Notably, during the pressurization, the sample changed from its initial black color to a rusty, metallic golden color (Figure 1D). This NC-coining technique can be generalized to produce coins from metal NCs with different sizes, shapes (sphere, cube, and rod), native ligands (polar and nonpolar molecules, as well as polymers), and compositions (gold, palladium, silver, platinum, rhodium, and bismuth) (Figures 1E-1K).

Optical Properties and Crystal Domains of NC Coins

One striking result of the coining process is the change in sample appearance, as the materials change from an absorption-dominant condition to a reflection-prevailing state (Figures 1C–1K; see also Figures S4 and S5). The absorption spectrum of the as-synthesized DDT-capped gold NCs (6.5 nm in diameter) in toluene showed a peak located at 519 nm, which was attributed to the localized surface-plasmon resonance (LSPR) (Figure 2A). After replacing DDT with inorganic ligands (i.e., S²⁻), the LSPR peak showed a redshift by 49 meV (~11 nm) due to both the NC surface charge redistribution and an increased dielectric constant of the solvent (toluene versus

¹Department of Chemistry, Brown University, Providence, RI 02912, USA

²Research Center of Integrative Molecular Systems (CIMoS), Institute for Molecular Science, Okazaki, Aichi 444-8585, Japan

³School of Engineering, Brown University, Providence, RI 02912, USA

⁴Center for Nanoscale Materials, Argonne National Laboratory, Argonne, IL 60439, USA

⁵Department of Geology, Brown University, Providence, RI 02912, USA

⁶Cornell High Energy Synchrotron Source, Cornell University, Ithaca, NY 14853, USA

⁷Department of Chemistry, University of Utah, Salt Lake City, UT 84112, USA

⁸Lead Contact

^{*}Correspondence: ouchen@brown.edu https://doi.org/10.1016/j.chempr.2020.12.026





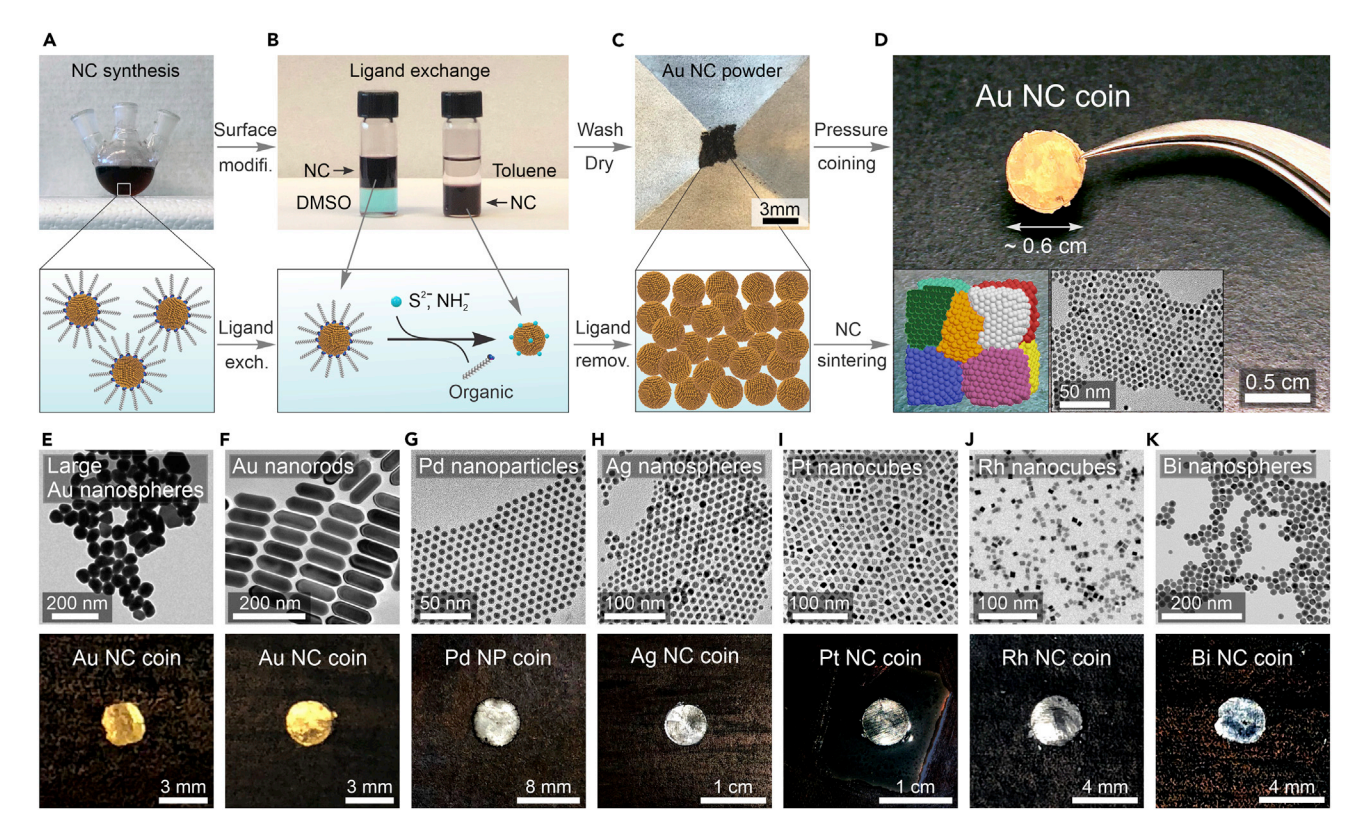


Figure 1. Fabrication of Metal NC Coins

- (A-D) Schematic of the NC-coining process.
- (A) Colloidally synthesized DDT-capped gold NCs dispersed in toluene.
- (B) Ligand exchange from native organic to inorganic ligands, transferring NCs from a nonpolar phase (toluene) to a polar solvent (DMSO).
- (C) A photograph of gold NC powder.
- (D) A photograph of a NC coin made from 6.5 nm gold NCs. Insets: a model of nanometer-sized GB condition (left) and a TEM image of the original gold NCs (right).
- (E-K) TEM images of the metal NCs (top) and photographs of the corresponding NC coins (bottom).
- (E) Gold nanospheres (61 nm).
- (F) Gold nanorods (40-nm width and 111-nm length).
- (G) Palladium nanoparticles (6.3 nm).
- (H) Silver nanospheres (9.5 nm).
- (I) Platinum nanocubes (8.4 nm).
- (J) Rhodium nanocubes (7.3 nm).
- (K) Bismuth nanospheres (18.9 nm).

DMSO) (Figures S1 and S8; Table S3). ^{24,26} The high absorption coefficient of the LSPR is consistent with the black color of the resulting NC powder after drying (Figure 1C; see also Figure S4). After NC coining, electrons can freely move across nanodomains within the gold NC coin, preventing electron localization and thus diminishing LSPR. Alternately, a new surface-plasmon polariton mode was observed in the NC coin as a result of the interactions between the surface delocalized electrons and the air, ²⁶ leading to the observed metallic color (Figures 1D–1K). Consistent with its golden appearance, reflectance measurements of the obtained gold NC coin showed a high reflectivity at long wavelengths (~ 600 nm) accompanied by a characteristic drop at approximately 500 nm (Figure 2B).

Despite the dramatic change in material appearance caused by the NC-coining process, all the NC coins made from different metal NCs with various sizes and shapes retained their original, nanometer-sized crystal domains (Figures 1D–1K; see also





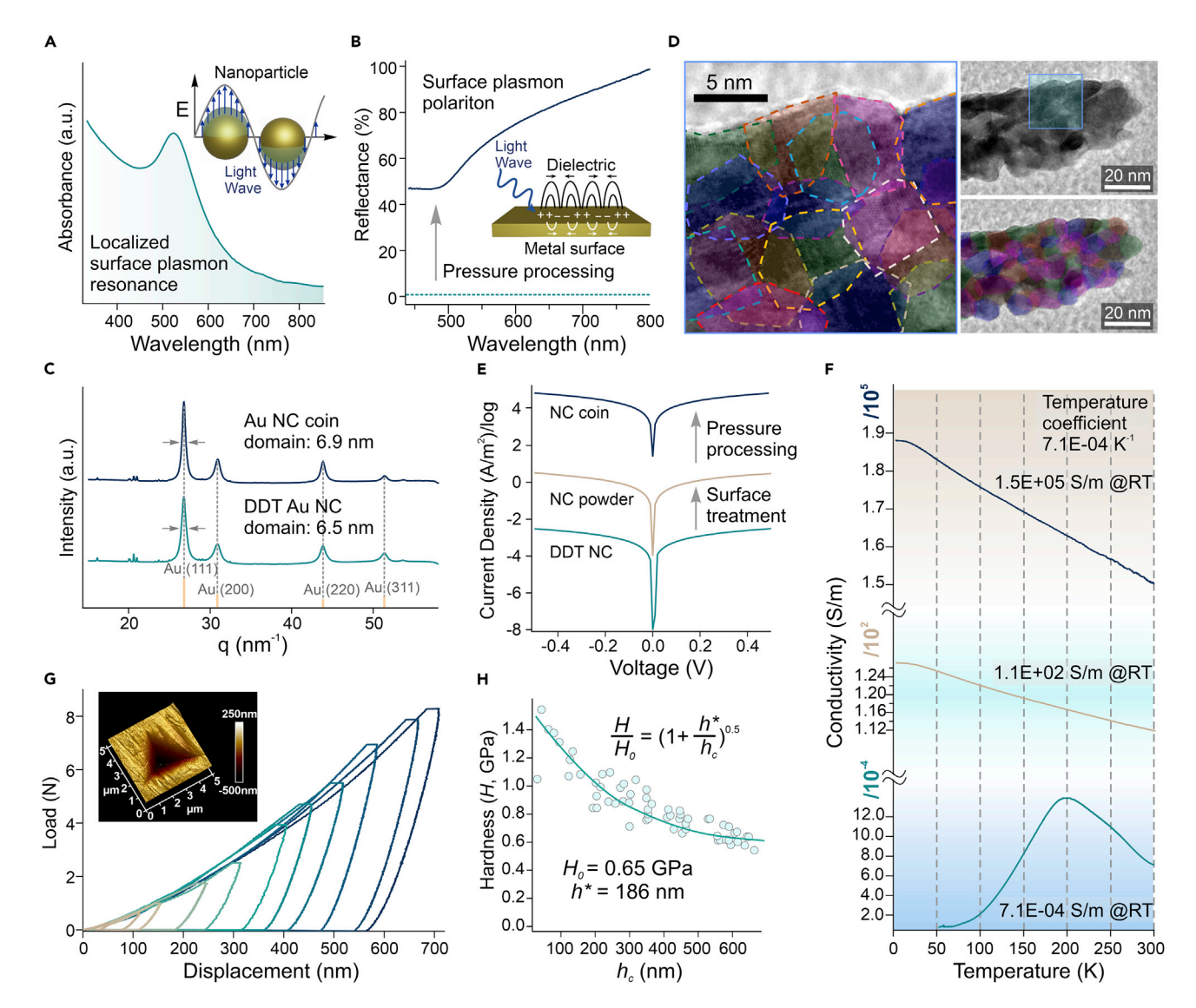


Figure 2. Characterizations of Gold NC Coin

- (A) UV-vis absorption spectrum of the original DDT-capped 6.5 nm gold NCs dispersed in toluene, exhibiting a LSPR (inset).
- (B) Reflection spectra of gold NC powder (green) and gold NC coin (blue). The gold NC coin exhibits a surface-plasmon polariton mode (inset).
- (C) XRD spectra of the original DDT-capped gold NCs (green) and the resultant gold NC coin (blue).
- (D) HR-TEM image of a thin piece of the gold NC coin with color-coded crystal domains (see the details in Supplemental Information).
- (E) I-V curves of the original DDT-capped gold NCs (green), gold NC powder (yellow) and gold NC coin (blue).
- (F) Plots of electric conductivity as a function of temperature for the original DDT-capped gold NCs (green), the gold NC powder (yellow), and gold NC coin (blue).
- (G) Representative load-displacement (h-P) curves from nanoindentation measurements of the gold NC coin. Inset: a 3D atomic force microscopy image of an indentation from the measurement.
- (H) A plot of hardness (H) as a function of the indentation depth showing data from 64 nanoindentation measurements.

Figures S9–S19; Tables S4–S10). X-ray diffraction (XRD) patterns of the DDT-capped gold NCs and gold NC coin showed almost identical profiles with unchanged grain sizes based on a Scherrer analysis (6.5 \pm 0.6 nm for the DDT-capped gold NCs versus 6.9 \pm 1.2 nm for the gold NC coin) (Figure 2C; see also Figure S9; Table S4). High-resolution transmission electron microscopy (HR-TEM) measurements confirmed that the crystal domain sizes of the NC coin were close to the size of the original gold NCs (Figure 2D; see also Figures S20–S22). Moreover, the crystal





domains were oriented randomly with respect to each other, suggesting that a fusion of gold NCs occurred during the coining process irrespective of the lattice orientation of the NCs (Figure 2D; see also Figures S20–S22). ^{13,16,18,21,22}

Electrical Transport Properties of NC Coins

Next, we characterized the electrical transport properties of the NC coins. Figure 2E shows current-voltage (I-V) curves for the gold NC coin, as well as two control samples: a gold NC pellet made from pressurized DDT-capped gold NCs and the unpressurized gold NC powder (see Methods S3; Figure S23; Table S11). The gold NC coin possessed a conductivity of 1.5×10^5 S/m at room temperature (300 K), among the highest conductivity values previously reported for the materials fabricated from colloidal gold NCs (Table S12). The lower conductivity of the NC coin compared with bulk gold (4.4×10^7 S/m) can be attributed to the increased number of scattering centers for conducting electrons at the GBs inside the NC coin. However, the conductivity values of pellets made from DDT-capped gold NC (7.1×10^{-4} S/m) and of the unpressurized gold NC powder (1.1×10^2 S/m) were substantially smaller than that of the gold NC coin by eight and three orders of magnitude, respectively (Figure 2E; see also Figure S23; Table S11). The essential factors in the metallization of NC building blocks.

To further characterize the NC coins, we performed temperature-dependent conductivity measurements (Figure 2F; see also Figures S23 and S24). The gold NC coin exhibited a linear decrease of conductivity with a temperature coefficient of $7.1\times 10^{-4}\,\rm K^{-1}$ upon heating from 20 to 300 K, validating the metallic electrical transport behavior as described by Matthiessen's rule (the scattering of electrons by acoustic phonons). In contrast, the DDT-capped gold NC pellet exhibited a metal-insulator transition curve with a turning temperature of 198 K (Figure 2F), in line with previous reports. The unpressurized gold NC powder also showed weak metallic behavior with a smaller temperature coefficient of $4.2\times 10^{-4}\,\rm K^{-1}$ at 20–300 K, indicating weak metallic contacts between NCs already exist in the powder due to the successful removal of ligands (Figure 2F; see also Table S11). Similar enhancements in electrical transport properties were also observed in a silver NC coin (with a conductivity value of $3.2\times 10^4\,\rm S/m$ at 300 K and a temperature coefficient of $1.7\times 10^{-4}\,\rm K^{-1}$ at 30–300 K; see also Figure S24; Table S11), demonstrating the metallic nature of the obtained materials.

Mechanical Properties of NC Coins

We conducted nanoindentation measurements to assess the mechanical properties of the NC coins (see Methods S4; Figures 2G and 2H; see also Figures S25 and S26). 29,30 Our gold NC coin exhibited hardness (H) values of 1.4–0.6 GPa in a contact depth (h_c) range of 50–600 nm (Figure 2H), more than 2- and 4-fold increases, respectively, over the reported values for single-crystalline (\sim 0.6 GPa), 31 and polycrystalline (\sim 0.3 GPa) gold at a contact depth of \sim 50 nm. 30 The improved hardness of our NC coins can be explained by GB strengthening, i.e., the Hall-Petch effect: the propagation of dislocations, responsible for plastic deformation, is impeded by a high density of GBs. 9,32 The decrease of hardness (H) with increasing depth of indentation depth (h_c) was attributed to the well-known indentation size effect and is well described by the relation $H/H_0 = (1+h^*/h_c)^{0.5}$, where H_0 is the intrinsic hardness and h^* is a length scale that characterizes the dependence of the depth on the hardness. 9,30,33 The best fit to our data is obtained with $H_0 = 0.65$ GPa and $h^* = 186$ nm (Figure 2H). Despite the large hardness value of the gold NC coin, the measured reduced Young's modulus (E_r) of 23 \sim 35 GPa was markedly lower than the reported value of \sim 80 GPa obtained





by nanoindentation for typical gold specimens (Figure S25).³⁰ These characteristic mechanical properties are consistent with the GB configuration of our gold NC coin.³⁴ We observed similar trends in the silver NC coins (Figure S26), validating the GB strengthening effect created by NC coining.

Single-Component Bulk Metallic Glass

Metallic glasses are metals that lack crystallinity. $^{12,23,35-38}$ To date, most reported metallic glasses are intermetallic alloys made via rapid condensation processes. $^{12,23,35-38}$ Single-component metallic glasses are notoriously difficult to produce due to the strong crystallization tendency of pure metals. 39 However, single-component Pd NPs can be fabricated in an amorphous state owing to the large surface energy of the particles. 40 Using our NC-coining process, we have successfully produced a single-component bulk-Pd metallic glass starting from such amorphous Pd NPs (Figures 3A–3E). Consistent with the amorphous phase of the NPs before coining, the XRD pattern of the obtained Pd coin did not show any additional features other than the short-range diffraction at a q-value of ~ 28 nm $^{-1}$, confirming its glassy state (Figure 3C). Both scanning electron microscopy and scanning TEM measurements showed that the Pd coin consisted of densely packed granular nanostructures with no sign of ligand (i.e., NH $_2$) incorporation (Figures 3D and 3E; see also Figures S27–S30). Furthermore, selected-area electron diffraction showed only a diffuse signal, unambiguously proving the amorphous structure of the Pd coin (Figure 3E; see also Figure S28).

The Pd coin exhibits a dramatically improved electric conductivity of 1.0 \times 10⁵ S/m compared with a pressurized organic-capped Pd NP pellet and the unpressurized Pd NP powder (Figure 3G; see also Figure S31; Table S11). In addition, the temperature dependence of the electric conductivity with a coefficient of 1.6 \times 10⁻⁴ /K confirms the metallic state of the Pd coin (Figure 3G; see also Figure S31; Table S11). All these characteristics unequivocally demonstrated the metallic and glassy nature of the Pd coin, which represents the first example of "bottom-up" creation of singlecomponent bulk metallic glass. We further characterized the mechanical properties of the Pd coin and compared them with those of a face-centered cubic (fcc) crystalline Pd foil (0.1 mm thick, 99.9 % purity, 25 × 25 mm) (Figures 3H–3K; see also Figures S32 and S33). Consistent with previous reports, we obtained values of 2.4 \pm 0.5 GPa and 137 \pm 13 Gpa, respectively, for the hardness value (H) and reduced Young's modulus (E_r) of the crystalline Pd foil (Figures 3I and 3J; see also Figure S32). 41 In contrast, the Pd coin had a similar hardness value of 2.6 \pm 0.5 GPa but a much smaller reduced Young's modulus of 37 \pm 7 GPa (Figures 3I and 3J; see also Figure S33). Similar reductions in Young's modulus values were observed by Sakai et al. as decreasing the grain size of crystalline Pd sample down to 5–15 nm range. 42 The ratio of hardness to reduced Young's modulus (H/E_t) is an important characteristic value that describes the friction and wear behavior of materials. ⁴³ The value of this ratio is approximately four times larger for the glassy Pd coin compared with the crystalline Pd foil (7.1% versus 1.8%) (Figure 3K). This unique mechanical property was attributed to the unprecedented structural features of the sample. 44

Pressure-Driven Sintering and Molecular Dynamics Simulations

Apart from fusions of NCs by melting, ^{45,46} two mechanisms of NC sintering have been previously documented, i.e., oriented attachment ^{14,15,17,19,47–51} and random fusion. ^{13,16,18,20,21} While oriented attachment (i.e., the fusion of NCs with identical lattice orientation) is mainly observed in ionic NCs (e.g., CdTe, PbS, CsPbBr₃), pressure sintering of metal NCs typically leads to fusion of NCs with randomly oriented lattices (see also Table S13). The preservation of original crystalline domain feature of NCs shown in this study is consistent with these previous reports. In addition, pressure





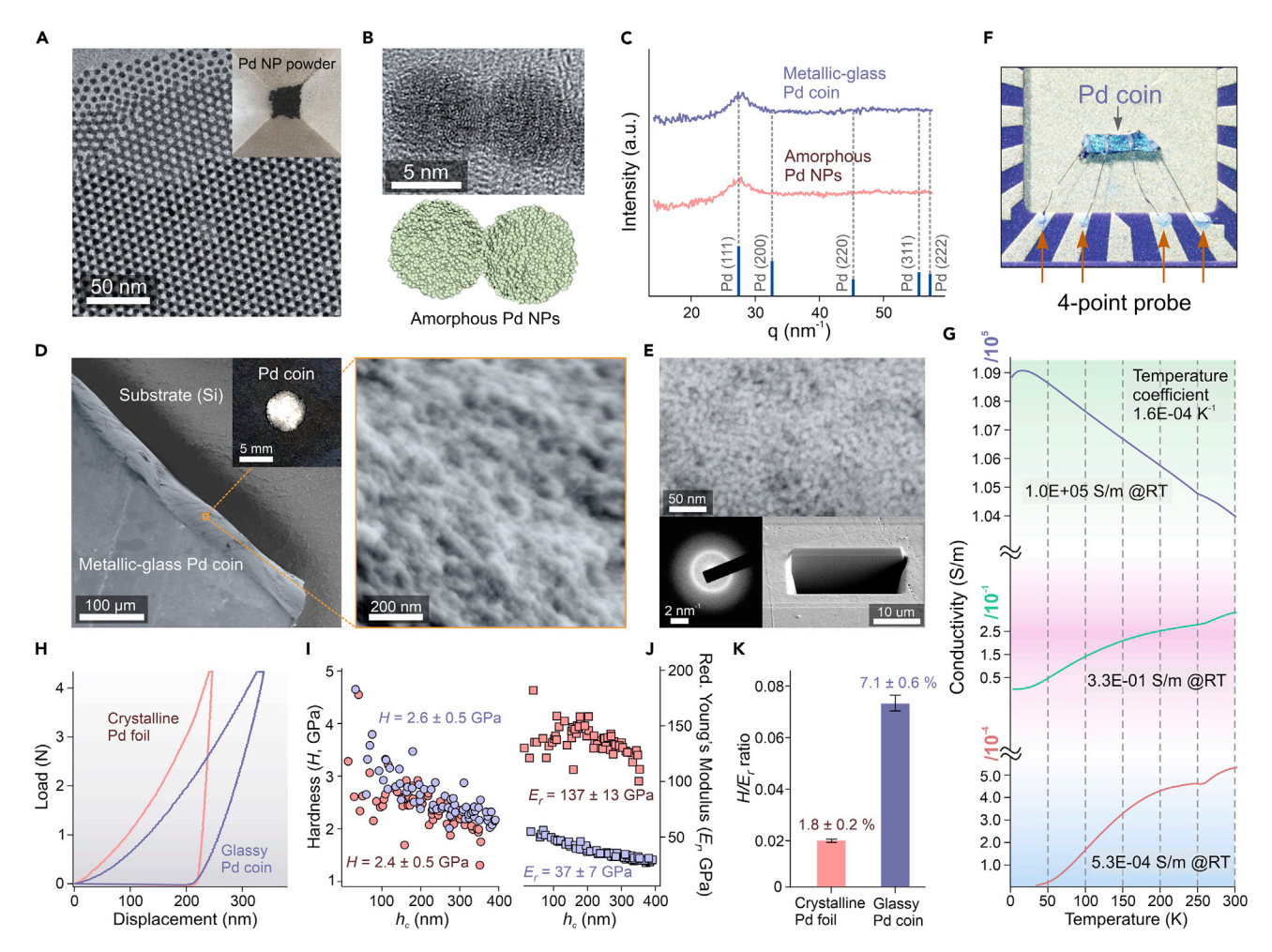


Figure 3. Characterizations of the Metallic-Glass Pd Coin

- (A) A TEM image of the amorphous Pd NPs capped with organic ligands. Inset: a photograph of Pd NP powder.
- (B) A HR-TEM image of the Pd NP capped with NH₂⁻, showing no atomic lattice fringes.
- (C) XRD spectra of the Pd NPs capped with NH2-.
- (D) SEM images of the Pd coin with a low (left) and a high magnification (right). Inset: a photograph of the Pd coin.
- (E) A STEM image of a Pd coin thinly sliced by a focused ion beam (FIB) (top), the corresponding selected-area electron diffraction (bottom left), and an SEM image of the surface area of Pd coin cut by FIB (bottom right).
- (F) A photograph of a piece of Pd coin in the 4-point probe setting for electric conductivity measurements.
- (G) Plots of electric conductivity as a function of temperature for the original Pd NPs capped with organic ligands (pink), the Pd NP powder (green), and the Pd coin (blue).
- (H) Representative load-displacement (h-P) curves from nanoindentation measurements for crystalline Pd foil (pink) and glassy Pd coin (blue).
- $(I\ and\ J)\ Plots\ of\ hardness\ (I)\ and\ reduced\ Young's\ modulus\ (J)\ as\ a\ function\ of\ indentation\ depth,\ showing\ data\ from\ 64\ nanoindentation\ measurements.$
- (K) H/E, (hardness/reduced Young's modulus) ratios for crystalline Pd foil and glassy Pd coin. The error bars represent standard deviations.

sintering of NCs capped with organic ligands requires pressures exceeding 10 GPa, where (partial) ligand detachment is observed. 13–15,18–20 At these pressures, the detached ligands segregate to form templates that guide the fusion of NCs into low-dimensional morphologies, including nanorods, nanowires, or nanoplatelets. 13–16,19,20,22 In our case, since NCs are essentially surfactant free, only a mild pressure of ~0.6 GPa, rather than large directional deviatoric stress, was employed to sinter NCs, 13,19 allowing for consolidation of the NCs. In fact, the pressure required to induce sintering of NCs is much lower than 0.6 GPa due to the high-energy surfaces of bare NCs. We universally applied the maximum safe pressure of our homemade pressure setup (i.e., 0.6 GPa) to reduce void spaces inside the NC powders and to provide



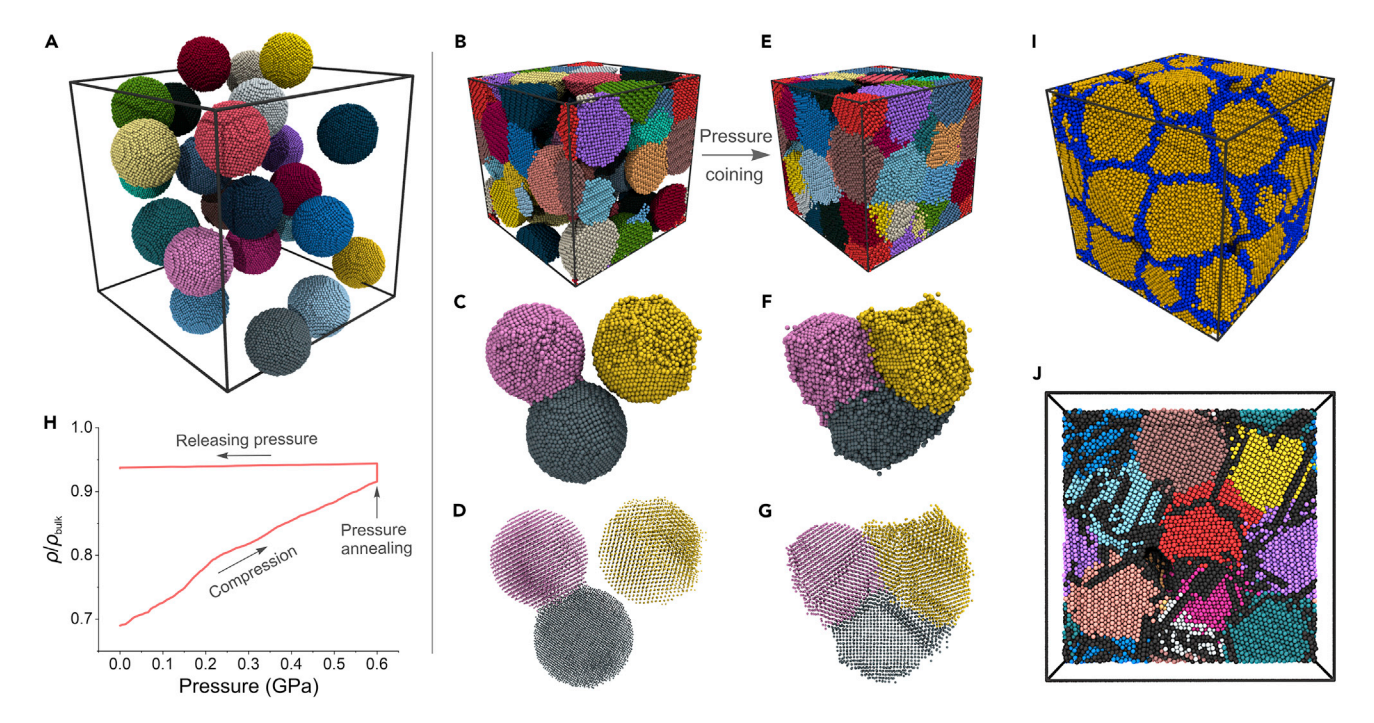


Figure 4. Molecular Dynamics Simulations of NC Coining

(A) Initial configuration of 27 spherical gold NCs.

(B–G) Snapshots of NC system (B and E) and three NCs (C, D, F, and G) at 1 atm and 300 K, before (B–D) and after compression to 0.6 GPa (E–G). In (D) and (G), gold atoms are shown in smaller size to reveal the domain structure of the NCs. In (B–G), gold atoms are color-coded according to the NC from which they originate in (A).

(H) A plot of the density of the NC system, relative to the density ρ_{bulk} of bulk gold, as a function of pressure during the coining process.

(I) A slice through the final NC coin, illustrating zones (ρ) of sintering between different NCs. Atoms with at least one nearest neighbor from a different NC are highlighted in blue color; atoms that are still surrounded exclusively by neighbors from the same NC are shown in gold color.

(J) A slice through the final coin, illustrating the grain-boundary structure. Atoms in GB (i.e., local environments that deviate substantially from a bulk FCC crystal; see Experimental Procedures) are shown in dark gray color; atoms in pristine local FCC environments are colored according to the NC they originated in.

maximum contact between NCs by increasing the density of the final bulk materials, resulting in bulk GB materials with dense metallic structures. 52

To further investigate the formation process and microscopic structure of NC coins, we simulated the coining process of 27 spherical single-crystal-domain fcc gold NCs with an average diameter of 6.5 nm (see Experimental Procedures). These gold NCs were initially placed in random disordered positions in a periodically replicated simulation box and the crystal lattices of individual NCs were randomly oriented with respect to each other (Figure 4A). When the NC system was equilibrated at ambient conditions, we observed local fusion of NCs around points of close contact (Figures 4B-4D), but NCs retained their spherical shapes with large voids between particles. When the pressure of this NC "powder" was subsequently raised to 0.6 GPa, the NCs sintered almost completely, resulting in a nearly void-free bulk gold system (Figures 4E-4G; see also Figure S34; Video S1). Consistently, the density (ρ) of the system increased drastically to \sim 94% of that of single-crystalline bulk gold (ho_{bulk}) and remained essentially unchanged upon pressure release (Figure 4H; see also Figure S35). We have verified that the final density of the NC coin is insensitive to the number of NCs used in simulations and that it depends only weakly on the packing density of NCs before coining (Figures S36 and S37).





During compression, some NCs change their shape markedly as they fill the available space (Figures 4C and 4F). These shape changes are mainly realized via slippage of (111) gold planes and through substantial reconstruction close to the NC surface (Figures 4D and 4G). To elucidate the microscopic structure of GBs in NC coins, we performed two types of analyses. First, we identified all atoms that, after pressure sintering, have established nearest-neighbor bonds with atoms that originally resided in different NCs, as illustrated in Figure 4I. As evident from the image, zones of sintering between pairs of different NCs are typically 2–3 atomic monolayers thick but can be more extended in places where several NCs approach closely. These sintering zones, however, do not always coincide with GBs. In fact, our simulations show that during pressure treatment new grains can form and extend across the sintering zones between originally distinct NCs. Figure 4J illustrates the location of GBs in a slice through a final NC coin (also see Experimental Procedures). While GBs (i.e., contiguous regions of gray atoms in Figure 4J) tend to be located at the boundaries between different NCs, the image also clearly reveals that pairs and triplets of NCs can form single FCC grains during sintering. Our simulations therefore reveal two competing processes that occur simultaneously during coining: the formation of new GBs, created as the nearly spherical NCs deform under pressure to form a compact material, and the consolidation of originally distinct NCs into single crystal grains. These observations are consistent with our XRD measurements that show no statistically significant change in grain size. Compared with our simulations, NC coining happens on much longer timescales in our experiments. It is therefore possible that the microscopic structure of real NC coins is consolidated via additional microscopic reconstruction that occurs on timescales inaccessible to our simulations.

Conclusions

In summary, we developed a "bottom-up" method to fabricate free-standing bulk GB materials from a library of metal NCs. Using this method, we created the first singlecomponent bulk metallic glass from amorphous Pd NPs. Owing to the nanometer-sized domains, the obtained NC coins showed electrical transport behaviors akin to those of bulk metals and improved mechanical properties. Importantly, the crystal grains in the final coin are directly determined by the NC sample used, which, owing to modern colloidal synthetic techniques, can be prepared with exquisitely narrow size and shape distribution and controlled composition. In addition, NC coining is operationally straightforward and fabrication conditions are mild. These advantages should facilitate the application of NC coining to other materials systems and on much larger production scales. Moreover, unlike many other methods, NC-coining produces free-standing GB materials—no substrate is needed. For these reasons, we expect that NC coining will be applied in the fabrication of a variety of GB materials that cannot be easily produced by existing techniques. We thus anticipate that our study will lead to new GB materials with diverse compositions (e.g., metals, oxides, semiconductors, and combinations), different domain sizes and shapes, tunable interfacial properties, and distinct crystal phases. Potential applications of such GB materials range from superhard materials, to thermoelectric generators and electrodes.

EXPERIMENTAL PROCEDURES

Resource Availability

Lead Contact

Further information and requests for additional details should be directed to and will be fulfilled by the Lead Contact, Ou Chen (ouchen@brown.edu).

Materials Availability

The materials generated in this study will be made available on request.





Data and Code Availability

All data in the Manuscript and Supplemental Information are available from the Lead Contact on request.

NC Synthesis

6.5 nm Gold NCs (DDT-Capped)

The synthesis of gold NCs followed a previously reported method. ⁵³ Briefly, 480 mg (Ph₃P)AuCl, 0.5 mL 1-DDT, and 80 mL benzene were loaded into a round-bottom flask. Under nitrogen blanket, the solution was heated to 75°C, and 881 mg *tert*-butylamine-borane (TBAB) was swiftly added to the flask. The reaction solution changed in color from transparent (pale yellow) to dark burgundy immediately after the injection. After maintaining the temperature for 1 h, the reaction was quenched by cooling using a water bath. The resulting gold NCs were crashed out of solutions using acetone and ethanol and collected through centrifugation. The resulting gold NCs were readily dispersed in toluene and stored for their use in the next step.

61 nm Gold Nanospheres (Citrate-Capped)

Gold nanospheres with an average diameter of 61 nm were synthesized via the Turkevich method. A typical synthesis is as follows: 7.94 mg sodium citrate was dissolved in 50 mL distilled H_2O in a flask and heated to boiling under continuous stirring. Then, $300\,\mu\text{L}$ of $HAuCl_4$ aqueous solution (0.08 M) was injected into the boiling solution. After 30 min reaction, the product was purified through centrifugation. The resulting gold nanospheres were stored in water for their use in the next step.

40-nm Width and 111-nm Length Gold Nanorods (CTAB-Capped)

Gold nanorods were made by a CTAB-assisted seeded growth approach. 54 Seed solutions were prepared as follows: 5 mL of HAuCl₄ · 3 H₂O aqueous solution (0.5 mM) and 5 mL of CTAB aqueous solution (0.2 M) were mixed in a 20 mL vial. Subsequently, the mixture was stirred for several minutes at 3 O°C in a water bath before adding 0.6 mL of 0.01 M fresh NaBH₄ aqueous solution. The seed solution was aged at 3 O°C for 3 O min.

Next, 2.7 g of CTAB and 0.3702 g of sodium oleate dissolved in 75 mL of distilled water were placed in a flask, and the solution was stirred for 20 min at 80°C. The solution was cooled down to 30°C followed by an addition of 5.4 mL AgNO3 aqueous solution (4 mM). After 20 min, 75 mL of HAuCl4 aqueous solution (1 mM) was injected. The mixture was kept at the same temperature for 1.5 h, and then, 4.5 mL of HCl aqueous solution was injected and further stirred for 15 min. Finally, 3.75 mL of ascorbic acid aqueous solution (0.064 M) and 120 μ L seed solution were swiftly added, and the resultant mixture was kept undisturbed at 30°C for 12 h. The product was purified through centrifugation. The resulting gold nanorods were stored in water for their use in the next step.

6.3 nm Amorphous Palladium NPs (OAm/TOP-Capped)

The synthesis of palladium NPs was conducted by following a previously reported heating-up method with a minor modification. ⁵⁵ Typically, 407 mg Pd(acac)₂, 4 mL TOP, and 40 mL OAm were placed into a round-neck flask. The mixture was degassed at room temperature for 1 h under vacuum. The reaction solution was then heated to 280°C under nitrogen slowly (c.a. 3°C/min) and was kept at 280°C for 30 min. Then, the reaction was quenched by removing the heating mantle and blowing cool air. The product was purified through centrifugation after precipitation with ethanol. The resulting palladium NPs were stored in toluene for their use in the next step.





9.5 nm Silver NCs (OAm-Capped)

Silver NCs were synthesized according to a reported method with minor modifications. ⁵⁶ Specifically, in our experiment, in order to enhance the crystallinity and size uniformity of the silver NCs, an annealing treatment and size-selective precipitation were introduced following the synthesis of silver NCs.

 $10\,\mathrm{mL}$ of OAm was loaded into a $50\,\mathrm{mL}$ flask and degassed under vacuum at $50^\circ\mathrm{C}$ for 1 h. The reaction solution was then heated to $180^\circ\mathrm{C}$ under nitrogen, and $500\,\mathrm{mg}$ of $\mathrm{AgNO_3}$ was swiftly added. Right after the addition, the color of the solution changed from colorless to dark orange. After $10\,\mathrm{min}$, the reaction solution was cooled down to room temperature (RT), and the product was collected through centrifugation following precipitation by acetone.

The product was dispersed in 10 mL toluene. The solution was heated to reflux and kept for 4 h before the reaction solution was cooled down to RT. Uniform NCs were collected by centrifugation and stepwise addition of acetone. The final product was stored in toluene for use in the next step.

8.4 nm Platinum NCs (OAm-Capped)

Platinum NCs were synthesized via a decomposition reaction of Pt(acac) $_2$. ⁵⁷ Typically, 400 mg Pt(acac) $_2$, 4 mL OAcid, 4 mL OAm, and 20 mL ODE were loaded into a 100 mL flask. The mixture was degassed under vacuum for 1 h and then heated to 60°C to allow the chemicals to be dissolved. The solution was heated up to 145°C. In another vial, 0.4 mL Fe(CO) $_5$ was mixed with 4 mL anhydrous hexane under an inert condition. Subsequently, the Fe(CO) $_5$ solution was swiftly injected into the reaction solution and kept at 145°C for 2 h for further reaction. The reaction was quenched by removing the heating mantle and blowing cool air. The product was collected through centrifugation following precipitation by ethanol. The resulting platinum NCs were stored in toluene for their use in the next step.

7.3 nm Rhodium NCs (PVP-Capped)

The synthesis of rhodium NCs followed a previously reported method. ⁵⁸ Typically, 53 mg of L-ascorbic acid, 107 mg of KBr, and 7 mL ethylene glycol were loaded into a 100 mL flask. The solution was heated up to 110°C and kept for 2 h under air (solution A). Meanwhile, 72 mg of Na₃RhCl₆ and 122 mg of polyvinylpyrrolidone (PVP, average mol. wt 40,000) were dissolved in 6 mL ethylene glycol, separately (solution B and C). The solution A was heated up to 140°C, and solution B and C were injected at the rate of 60 mL/h in the first 1 min (1 mL), and at the rate of 4 mL/h after the first 1 min. The reaction was quenched by removing the heating mantle and blowing cool air, followed by centrifugation after mixing the reaction solution with acetone and ethanol. The resulting rhodium NCs were stored in methanol for their use in the next step.

18.9 nm Bismuth NCs (DDT-Capped)

Bismuth NCs were made by a reported method with minor modifications. ⁵⁹ 1.54 g Bi(nda) and 10 mL ODE were loaded in a flask, and the solution was degassed under vacuum at 80°C. Subsequently, 0.5 mL DDT and 0.5 mL OAm were added into the solution. The solution was heated up to 80°C followed by an injection of 4 mL TOP. The reaction solution was kept at 75°C for 100 s, and then the reaction was quenched using an ice-water bath. The crude product was collected through centrifugation, followed by another round of washing process using tetrahydrofuran (THF) as a good solvent and acetone as a bad solvent. The final product was stored in THF for their use in the next step.





Surface Treatment and Drying of NCs

The reactivity between the inorganic NC core and replacing inorganic ligand is important for this ligand exchange/removal process. Proper inorganic ligands must be carefully selected depending on the NC core component. NCs should be moderately inert under the ligand exchange conditions, and the resulting surface should be intact. In addition, complete purification and thorough drying of the resulting NCs after ligand exchange are important steps in the NC-coining process. The detailed ligand-exchange procedure for each NC cases are described below:

(1) Ligand exchange with S^{2-} for hydrocarbon chain-tethered NCs in toluene (6.5 nm gold NCs and 18.9 nm bismuth NCs)

Ligand exchanges with S^{2-} were conducted as follows: $(NH_4)_2S$ was diluted to $0.1{\sim}0.05$ % in DMSO. A NC toluene solution was mixed with the solution and the mixture was vigorously stirred for 15 min. In order to extract the exchanged native surface ligand, two-layers extraction purification was employed; hexane was added to the mixture solution leading to two-phase liquid separation. The upper transparent layer contained hexane, toluene, and the native ligand (molecules with long hydrocarbon chains), the colored bottom layer consisted of polar components such as DMSO and S^{2-} capped NCs. The top layer was carefully removed. This process was repeated until the interface between the two layers became clear, which typically took 3–5 times. Acetone was added to the resulting NC-DMSO solution to crash out the NCs, followed by centrifugation at 12,000 rpm for 15 min. Multiple rounds of purification using DMSO and acetone were carried out. The collected powder sample was further washed by acetone for multiple times and dried completely under vacuum for several days, resulting the final NC powder.

(2) Ligand exchange with S^{2-} for water-dispersible NCs (61 nm gold nanospheres and 40–111 nm gold nanorods)

First, $(NH_4)_2S$ was diluted to 0.1% in DMSO. Then, 20 mL of the aqueous NC colloidal solution was mixed with 0.2 mL of $(NH_4)_2S$ DMSO solution and the mixture was stirred for 15 min until the surface reaction was completed. The solution was then centrifugated at 12,000 rpm for 15 min. The collected precipitate was readily dispersed in DMSO but could no longer be dispersed in water, indicating a successful ligand exchange with S^{2-} . The NCs were further washed using water and isopropanol for multiple rounds. The final product was further washed by isopropanol for multiple times and dried under vacuum for several days, resulting the dried NC powder.

(3) Ligand exchange for with NH₂⁻ for OAm-capped NCs (8.4 nm platinum, 6.3 nm palladium, 9.5 nm silver, and 7.3 nm rhodium NCs)

The procedure of ligand exchanges with NH_2^- was as follows; 20 mg of $NaNH_2$ was dissolved in 10 mL DMSO, followed by an addition of 10 mL of the colloidal sample solution. The mixture was stirred for 2 days to complete the ligand exchange. For purification of the NCs capped with NH_2^- , we employed a typical centrifugation method with nanopore water (good solvent) and acetone and/or isopropanol (bad solvent). The purification process was repeated twice. The resulting precipitate was further washed using acetone and/or isopropanol for multiple rounds. The final product was dried under vacuum for several days, resulting the dried NC powder.





Pressure-Induced NC-Coining Process

The pressurizing process in the NC-coining process was performed using a home-made piston cylinder. The pressure stage and piston cylinder are made of tungsten carbide. Force was applied using a pellet maker, and the pressure was calculated by dividing the applied force by the area of the cylinder. The photographs of a piston cylinder and the detailed experimental procedure are shown in the Supplemental Information.

Polishing NC Coins

For the reflectance and nanoindentation measurements, the surface of the samples was polished using the standard procedure described in *Metallographic Handbook* by PACE Technologies, USA (https://www.metallographic.com/). Typically, NC coins were attached to glass substrates using a thin layer of epoxy (Loctite Stycast). Next, 800 (P2400) grit SiC paper followed by P1200 grit ALO paper was used to flatten the sample surface using water as the lubricant. Subsequently, the sample was polished for 2 min using a 1-μm diamond powder on ATLANTIS polishing pad. Finally, the surface was polished using a 0.05-μm Nanometer alumina on NAP-PAD polishing pad.

Optical Properties Characterization

UV-vis absorption spectra were measured using an Agilent Technologies Cary 5000 UV-vis-NIR Spectrophotometer. The reflectance spectra were collected with the 508 PV Microscope Spectrophotometer (CRAIC Technologies). Prior to the reflectance measurement, the surface of the samples was sufficiently polished (see above session of "Polishing NC coins").

Electron Microscopy Measurement and Focused Ion Beam (FIB) Technique

TEM and electron diffraction measurements were performed on a JEOL-2100F operated at 200 kV and an FEI-Philips CM20 operated at 200 kV. Electron diffraction measurements were carried out on a JEOL-2100F operated at 200 kV. HAADF scanning TEM (STEM) was performed on an FEI Talos F200X TEM/STEM running at 200 kV.

SEM measurements were performed on a LEO 1530 operated at 3 kV. FIB technique was employed to prepare thin slice TEM samples and to create a hole to observe the cross-sectional structures of the coins using Thermo Scientific Helios NanoLab Dual Beam microscope

X-Ray Diffraction (XRD)

XRD measurements were performed on a Bruker D8 Discovery 2D X-ray Diffractometer equipped with a Vantec 500 2D area detector, and a Bruker D8 Discovery High-resolution X-ray Diffractometer with the operating voltage of 40 kV and the operation current 40 mA. X-ray from Cu-K α radiation with a wavelength of 1.541 Å was used.

Electrical Transport Measurements

For conductivity measurements, the samples were cut into small pieces with a typical dimension of tens to hundreds of micrometers (see also in the Supplemental Information). Standard four-point probe measurements were carried out with four gold wires (15 μ m Φ) attached with silver paste. Constant current (0.1 μ A \sim 10 mA) was applied by a 2636B source meter (Keithley), and the potential difference was measured by a 2182A nanovoltmeter (Keithley). All the measurements were performed under reduced He pressure in Physical Property Measurement System (PPMS) (Quantum Design) using a TTPX cryogenic probe station (Lakeshore). The





temperature was controlled by PPMS at a sweeping temperature rate of $0.1 \sim 1.0 \text{ K/min}$. The photographs of the setting are shown in the Supplemental Information.

Nanoindentation

Mechanical properties (reduced Young's modulus and hardness) of the samples were characterized by means of nanoindentation using a Berkovich tip integrated to a Hysitron Tribointenter (Model T900). Prior to the measurements, the samples were polished (see above session of "Polishing NC coins"). A total of 64 indentations (an array of 8 × 8) were conducted for each sample with following conditions: (1) The maximum load was varied between \sim 0.1 and \sim 8.0 mN at constant increments (\sim 0.12 mN), (2) The loading/unloading rate was kept constant (\sim 0.5 mN/s) for each indentation. (3) 2 s of holding time were inserted between the loading step and the unloading step. (4) The location of each indentation was separated by 10 µm.

The obtained load-displacement (h-P) curves were used to calculate the values of reduced Young's modulus (E_r) and hardness (H) using TRIBOINDENTER® SOFTWARE. The detailed explanation is described in the Supplemental Information.

Molecular Dynamics Simulations

To model interactions between gold atoms, we used the embedded-atom model by Foiles and coworkers, 60 as implemented in LAMMPS. 61 We created 27 NCs with different sizes by placing gold atoms on an fcc lattice with a lattice constant of $4.1\,\text{Å}$ within spherical regions of diameter (6.5+d) nm, where d was a random number drawn from a uniform distribution on the interval [-0.5;0.5]. The orientations of the 27 NCs were randomized and the NCs placed on disordered positions obtained from a simulation of 27 Lennard-Jones particles at a typical fluid density. NC positions were appropriately scaled to avoid overlap. We enclosed the system (213,156 atoms in total) by a periodically replicated cubic simulation box with an edge length of 34 nm. To simulate the production of a NC coin, the system was first equilibrated at constant volume for 0.125 ns at a temperature of 600 K (enforced by a Nose-Hoover thermostat with a time constant of 1 ps and a time step of 20 fs, as implemented in LAMMPS) and then for another 0.125 ns at 300 K. Then, using a Nose-Hoover thermostat (keeping a temperature of 300 K throughout) and barostat (with time constant of 1 ps), we further equilibrated the system at a pressure of 1 atm for 1.25 ns. We then linearly increased the pressure to 0.6 GPa over the course of 1.25 ns, followed by another 1.25 ns of equilibration at fixed pressure of 0.6 GPa. Finally, the pressure was reduced to 1 atm within 0.25 ns, and the system was equilibrated at ambient conditions for another 1.25 ns. All simulation images were produced using VMD.⁶²

To identify GBs, as illustrated in Figure 4J, we used the Steinhard order parameter q_4 , as implemented in LAMMPS. ⁶³ For atoms in perfect fcc environments, $q_4 \approx$ 0.19; we identify all atoms with $q_4 <$ 0.15 as non-crystalline, i.e., as part of a grain boundary. Histograms of q_4 in a bulk fcc crystal, a system of isolated NCs, and in a NC coin are shown in Figure \$38.

Analysis Software

A Multi-Peak Fitting 2.0 package in *Igor Pro* version 6.37 (WaveMetrics) was used for the XRD peak analyses. *ImageJ* (https://imagej.nih.gov/ij/) was used for TEM image analysis using 2D-fast Fourier transform (FFT) analysis, and an inverse FFT analysis functions.

Sample Size

No statistical methods were used to predetermine sample size.





SUPPLEMENTAL INFORMATION

Supplemental Information can be found online at https://doi.org/10.1016/j.chempr. 2020.12.026.

ACKNOWLEDGMENTS

Y.N. thanks A. McCormick, K. Talbot, and R. Goulet for their help for sample and device preparation. O.C. acknowledges the support from the Brown University Startup Fund and the NSF funds (DMR-1943930, CMMI-1934314). CHESS was supported by the NSF award DMR-1332208 and DMR-1829070. The TEM, SEM, and XRD measurements were performed at the Electron Microscopy Facility in the Institute for Molecular and Nanoscale Innovation (IMNI) at Brown University. Work by M.S and H.M.Y. was supported by Grant-in-Aid for Scientific Research on Innovative Areas (no. 19H04603) from the Japan Society for the Promotion of Science (JSPS) and a grant by the Noguchi institute. The support and resources of the Center for High Performance Computing at the University of Utah are gratefully acknowledged. Work by M.G. was supported by the National Science Foundation under grant no. DMR-1848499. Use of the Center for Nanoscale Materials, an Office of Science user facility, was supported by the U.S. Department of Energy, Office of Science, Office of Basic Energy Sciences, under contract no. DE-AC02-06CH11357.

AUTHOR CONTRIBUTIONS

Conceptualization and methodology, Y.N. and O.C.; Modeling, M.G.; Investigation, Y.N., N.C., H.Y., M.S., H.M.Y., I.Y., B.A., S.P., Y.L., and Z.W.; Writing, Original Draft, Y.N., M.G., and O.C.; Writing review and editing, all authors; Supervision, O.C.

DECLARATION OF INTERESTS

The authors declare no competing interests.

Received: May 25, 2020 Revised: September 25, 2020 Accepted: December 24, 2020 Published: January 22, 2021

REFERENCES

- 1. Lu, L., Sui, M.L., and Lu, K. (2000). Superplastic extensibility of nanocrystalline copper at room temperature. Science 287, 1463–1466.
- Lu, L., Shen, Y., Chen, X., Qian, L., and Lu, K. (2004). Ultrahigh strength and high electrical conductivity in copper. Science 304, 422–426.
- Mariano, R.G., McKelvey, K., White, H.S., and Kanan, M.W. (2017). Selective increase in CO₂ electroreduction activity at grain-boundary surface terminations. Science 358, 1187–1192.
- Watanabe, T. (2011). Grain boundary engineering: historical perspective and future prospects. J. Mater. Sci. 46, 4095–4115.
- Li, S., Cui, S., Chen, H., Li, J., Huang, H., and Luo, H. (2019). Effect of cooling rates on solidification, microstructure and mechanical properties in tungsten. CrystEngComm 21, 3930–3938.
- 6. Suryanarayana, C., and Prabhu, B. (2007). Synthesis of nanostructured materials by inertgas condensation methods. In Nanostructured Materials Processing, Properties, and

- Applications C.C. Koch 2nd Edition (Elvevier), pp. 47–90.
- Eckert, J., Holzer, J.C., Krill, C.E., and Johnson, W.L. (1993). Mechanically driven alloying and grain size changes in nanocrystalline Fe-Cu powders. J. Appl. Phys. 73, 2794–2802.
- Shan, Z.W., Adesso, G., Cabot, A., Sherburne, M.P., Asif, S.A., Warren, O.L., Chrzan, D.C., Minor, A.M., and Alivisatos, A.P. (2008). Ultrahigh stress and strain in hierarchically structured hollow nanoparticles. Nat. Mater. 7, 947–952.
- Van Swygenhoven, H. (2002). Polycrystalline materials. Grain boundaries and dislocations. Science 296, 66–67.
- Lu, K., Lu, L., and Suresh, S. (2009). Strengthening materials by engineering coherent internal boundaries at the nanoscale. Science 324, 349–352.
- 11. Pham, M.S., Liu, C., Todd, I., and Lertthanasarn, J. (2019). Damage-tolerant architected

- materials inspired by crystal microstructure. Nature *565*, 305–311.
- Thompson, R.L., Wang, Y.Q., and Greer, J.R. (2018). Irradiation enhances strength and deformability of nano-architected metallic glass. Adv. Eng. Mater. 20, 1701055.
- Wu, H., Bai, F., Sun, Z., Haddad, R.E., Boye, D.M., Wang, Z., and Fan, H. (2010). Pressuredriven assembly of spherical nanoparticles and formation of 1D-nanostructure arrays. Angew. Chem. Int. Ed. Engl. 49, 8431–8434.
- Wang, Z., Schliehe, C., Wang, T., Nagaoka, Y., Cao, Y.C., Bassett, W.A., Wu, H.M., Fan, H., and Weller, H. (2011). Deviatoric stress driven formation of large single-crystal PbS nanosheet from nanoparticles and in situ monitoring of oriented attachment. J. Am. Chem. Soc. 133, 14484–14487.
- Nagaoka, Y. (2013). Nanocrystal Superlattices: Synthesis and Characterization under High-Pressure (University of Florida).





- Li, B.S., Wen, X., Li, R., Wang, Z., Clem, P.G., and Fan, H. (2014). Stress-induced phase transformation and optical coupling of silver nanoparticle superlattices into mechanically stable nanowires. Nat. Commun. 5, 4179.
- Wang, T., Li, R., Quan, Z., Loc, W.S., Bassett, W.A., Xu, H., Cao, Y.C., Fang, J., and Wang, Z. (2015). Pressure processing of nanocube assemblies toward harvesting of a metastable PbS phase. Adv. Mater. 27, 4544–4549.
- Zhu, J., Quan, Z., Wang, C., Wen, X., Jiang, Y., Fang, J., Wang, Z., Zhao, Y., and Xu, H. (2016). Structural evolution and mechanical behaviour of Pt nanoparticle superlattices at high pressure. Nanoscale 8, 5214–5218.
- Nagaoka, Y., Hills-Kimball, K., Tan, R., Li, R., Wang, Z., and Chen, O. (2017). Nanocube superlattices of cesium lead bromide perovskites and pressure-induced phase transformations at atomic and mesoscale levels. Adv. Mater. 29, 1606666.
- Zhu, H., Nagaoka, Y., Hills-Kimball, K., Tan, R., Yu, L., Fang, Y., Wang, K., Li, R., Wang, Z., and Chen, O. (2017). Pressure-enabled synthesis of hetero-dimers and hetero-rods through intraparticle coalescence and interparticle fusion of quantum-dot-Au satellite nanocrystals. J. Am. Chem. Soc. 139, 8408– 8411.
- Li, B.S., Bian, K., Zhou, X., Lu, P., Liu, S., Brener, I., Sinclair, M., Luk, T., Schunk, H., Alarid, L., et al. (2017). Pressure compression of CdSe nanoparticles into luminescent nanowires. Sci. Adv. 3, e1602916.
- Bai, F., Bian, K., Huang, X., Wang, Z., and Fan, H. (2019). Pressure induced nanoparticle phase behavior, property, and applications. Chem. Rev. 119, 7673–7717.
- Adjaoud, O., and Albe, K. (2018).
 Microstructure formation of metallic nanoglasses: insights from molecular dynamics simulations. Acta Mater. 145, 322–330.
- 24. Nag, A., Kovalenko, M.V., Lee, J.S., Liu, W., Spokoyny, B., and Talapin, D.V. (2011). Metalfree inorganic ligands for colloidal nanocrystals: S²⁻, HS⁻, Se²⁻, HSe⁻, Te²⁻, HTe⁻, TeS₃²⁻, OH⁻, and NH₂⁻ as surface ligands. J. Am. Chem. Soc. 133, 10612–10620.
- Fafarman, A.T., Koh, W.K., Diroll, B.T., Kim, D.K., Ko, D.K., Oh, S.J., Ye, X., Doan-Nguyen, V., Crump, M.R., Reifsnyder, D.C., et al. (2011). Thiocyanate-capped nanocrystal colloids: vibrational reporter of surface chemistry and solution-based route to enhanced coupling in nanocrystal solids. J. Am. Chem. Soc. 133, 15753–15761.
- Barnes, W.L., Dereux, A., and Ebbesen, T.W. (2003). Surface plasmon subwavelength optics. Nature 424, 824–830.
- Doty, R.C., Yu, H., Shih, C.K., and Korgel, B.A. (2001). Temperature-dependent electron transport through silver nanocrystal superlattices. J. Phys. Chem. B 105, 8291–8296.
- Cargnello, M., Johnston-Peck, A.C., Diroll, B.T., Wong, E., Datta, B., Damodhar, D., Doan-Nguyen, V.V., Herzing, A.A., Kagan, C.R., and Murray, C.B. (2015). Substitutional doping in nanocrystal superlattices. Nature 524, 450–453.

- Pharr, G.M., Oliver, W.C., and Brotzen, F.R. (1992). On the generality of the relationship among contact stiffness, contact area, and elastic modulus during indentation. J. Mater. Res. 7. 613–617.
- Fischer-Cripps, A.C. (2011). Appendices 1–7. In Nanoindentation, Third Edition (Springer), pp. 235–276.
- Corcoran, S.G., Colton, R.J., Lilleodden, E.T., and Gerberich, W.W. (1997). Anomalous plastic deformation at surfaces: nanoindentation of gold single crystals. Phys. Rev. B 55, R16057– R16060.
- Holm, E.A., and Foiles, S.M. (2010). How grain growth stops: a mechanism for grain-growth stagnation in pure materials. Science 328, 1138–1141.
- Nix, W.D., and Gao, H.J. (1998). Indentation size effects in crystalline materials: a law for strain gradient plasticity. J. Mech. Phys. Solids 46, 411–425.
- 34. Zhou, Y., Erb, U., Aust, K.T., and Palumbo, G. (2003). The effects of triple junctions and grain boundaries on hardness and Young's modulus in nanostructured Ni-P. Scr. Mater. 48, 825–830.
- **35.** Telford, M. (2004). The case for bulk metallic glass. Mater. Today *7*, 36–43.
- Gleiter, H. (2013). Nanoglasses: a new kind of noncrystalline materials. Beilstein J. Nanotechnol. 4, 517–533.
- Ivanisenko, Y., Kübel, C., Nandam, S.H., Wang, C., Mu, X., Adjaoud, O., Albe, K., and Hahn, H. (2018). Structure and properties of nanoglasses. Adv. Eng. Mater. 20, 1800404.
- Zhong, L., Wang, J., Sheng, H., Zhang, Z., and Mao, S.X. (2014). Formation of monatomic metallic glasses through ultrafast liquid quenching. Nature 512, 177–180.
- An, Q., Luo, S.-N., Goddard, W.A., III, Han, W.Z., Arman, B., and Johnson, W.L. (2012). Synthesis of single-component metallic glasses by thermal spray of nanodroplets on amorphous substrates. Appl. Phys. Lett. 100, 041909.
- Liu, Y., Wang, C., Wei, Y., Zhu, L., Li, D., Jiang, J.S., Markovic, N.M., Stamenkovic, V.R., and Sun, S. (2011). Surfactant-induced postsynthetic modulation of Pd nanoparticle crystallinity. Nano Lett. 11, 1614–1617.
- Chalakova, G., Datcheva, M., Zaharieva, R., Georgiev, M., Dobrovolska, T.s., and Stoychev, D. (2015). Nanomechanical testing of thin composite layers—application to Pd-in Electrochemically Deposited Thin Films. AIP Conf. Proc. 1684, 030002.
- Sakai, S., Tanimoto, H., and Mizubayashi, H. (1998). Mechanical behavior of high-density nanocrystalline gold prepared by gas deposition method. Acta Mater. 47, 211–217.
- Ni, W.Y., Cheng, Y.-T., Lukitsch, M.J., Weiner, A.M., Lev, L.C., and Grummon, D.S. (2004). Effects of the ratio of hardness to Young's modulus on the friction and wear behavior of bilayer coatings. Appl. Phys. Lett. 85, 4028–4030.
- Grochala, W., Hoffmann, R., Feng, J., and Ashcroft, N.W. (2007). The chemical imagination at work in very tight places. Angew. Chem. Int. Ed. Engl. 46, 3620–3642.

- Goodfellow, B.W., Rasch, M.R., Hessel, C.M., Patel, R.N., Smilgies, D.M., and Korgel, B.A. (2013). Ordered structure rearrangements in heated gold nanocrystal superlattices. Nano Lett 13, 5710–5714.
- Cheng, F., Lian, L., Li, L., Rao, J., Li, C., Qi, T., Zhang, Z., Zhang, J., and Gao, Y. (2019). Hybrid growth modes of PbSe nanocrystals with oriented attachment and grain boundary migration. Adv Sci (Weinh). 6, 1802202.
- Tang, Z., Kotov, N.A., and Giersig, M. (2002). Spontaneous organization of single CdTe nanoparticles into luminescent nanowires. Science 297, 237–240.
- Penn, R.L., and Banfield, J.F. (1998). Imperfect oriented attachment: dislocation generation in defect-free nanocrystals. Science 281, 969–971.
- Boneschanscher, M.P., Evers, W.H., Geuchies, J.J., Altantzis, T., Goris, B., Rabouw, F.T., van Rossum, S.A.P., van der Zant, H.S.J., Siebbeles, L.D.A., Van Tendeloo, G., et al. (2014). Longrange orientation and atomic attachment of nanocrystals in 2D honeycomb superlattices. Science 344, 1377–1380.
- Schliehe, C., Juarez, B.H., Pelletier, M., Jander, S., Greshnykh, D., Nagel, M., Meyer, A., Foerster, S., Kornowski, A., Klinke, C., and Weller, H. (2010). Ultrathin PbS sheets by twodimensional oriented attachment. Science 329, 550-553
- Whitham, K., Smilgies, D.M., and Hanrath, T. (2018). Entropic, enthalpic, and kinetic aspects of interfacial nanocrystal superlattice assembly and attachment. Chem. Mater. 30, 54–63.
- Trappe, V., Prasad, V., Cipelletti, L., Segre, P.N., and Weitz, D.A. (2001). Jamming phase diagram for attractive particles. Nature 411, 772–775.
- Zheng, N., Fan, J., and Stucky, G.D. (2006). One-step one-phase synthesis of monodisperse noble-metallic nanoparticles and their colloidal crystals. J. Am. Chem. Soc. 128, 6550–6551.
- 54. Ye, X.C., Zheng, C., Chen, J., Gao, Y.Z., and Murray, C.B. (2013). Using Binary surfactant mixtures to simultaneously improve the dimensional tunability and monodispersity in the seeded growth of gold nanorods. Nano Lett. 13, 765–771.
- Kim, S.W., Park, J., Jang, Y., Chung, Y., Hwang, S., Hyeon, T., and Kim, Y.W. (2003). Synthesis of monodisperse palladium nanoparticles. Nano Lett. 3, 1289–1291.
- 56. Wang, D.S., Xie, T., Peng, Q., and Li, Y.D. (2008). Ag, Ag_2S , and Ag_2S e nanocrystals: synthesis, assembly, and construction of mesoporous structures. J. Am. Chem. Soc. 130, 4016-4022.
- 57. Wang, C., Daimon, H., Onodera, T., Koda, T., and Sun, S. (2008). A general approach to the size- and shape-controlled synthesis of platinum nanoparticles and their catalytic reduction of oxygen. Angew. Chem. Int. Ed. Engl. 47, 3588–3591.
- Zhang, H., Li, W., Jin, M., Zeng, J., Yu, T., Yang, D., and Xia, Y. (2011). Controlling the morphology of rhodium nanocrystals by manipulating the growth kinetics with a syringe pump. Nano Lett. 11, 898–903.

Chem Article



- 59. Son, J.S., Park, K., Han, M.K., Kang, C., Park, S.G., Kim, J.H., Kim, W., Kim, S.J., and Hyeon, T. (2011). Large-scale synthesis and characterization of the size-dependent thermoelectric properties of uniformly sized bismuth nanocrystals. Angew. Chem. Int. Ed. Engl. 50, 1363–1366.
- Foiles, S.M., Baskes, M.I., and Daw, M.S. (1986). Embedded-atom-method functions for the fcc metals Cu, Ag, Au, Ni, Pd, Pt, and their alloys. Phys. Rev. B Condens. Matter 33, 7983–7991.
- **61.** Plimpton, S. (1995). Fast parallel algorithms for short-range molecular dynamics. J. Comput. Phys. *117*, 1–19.
- 62. Humphrey, W., Dalke, A., and Schulten, K. (1996). VMD: visual molecular dynamics. J. Mol. Graph. 14, 27, 33–8.
- Steinhardt, P.J., Nelson, D.R., and Ronchetti, M. (1996). Bond-orientational order in liquids and glasses. Phys. Rev. B 28, 784–805.